Supporting Information

Enhancing Thermal Transport in TKX-50 Energetic Materials: The Role of Graphene Orientation and Molecular Interactions

Shuping Zhang,[1] Xiao Xu,[1,*] Xunjian Zhang,[1] Liqian Song,[1] and Xu Jia[1,†]

[1]*School of Chemistry and Chemical Engineering, Nanjing University of Science and Technology, 200 Xiao Ling Wei, Nanjing 210094, P. R. China*

[*] xuxiao@njust.edu.cn

[†] jiaxu@njust.edu.cn

I. COMPATIBILITY BETWEEN CHARGE DISTRIBUTION AND FORCE FIELD

Quantum calculation was performed to optimize the geometrical structure of TKX-50's ionic pairs with Gaussian 09 software, respectively. The Gaussian electrostatic potential (ESP) charges [1] of all atoms were obtained, as indicated in Fig. S1. HF/6-31G(d) provides sufficiently accurate charge distributions.

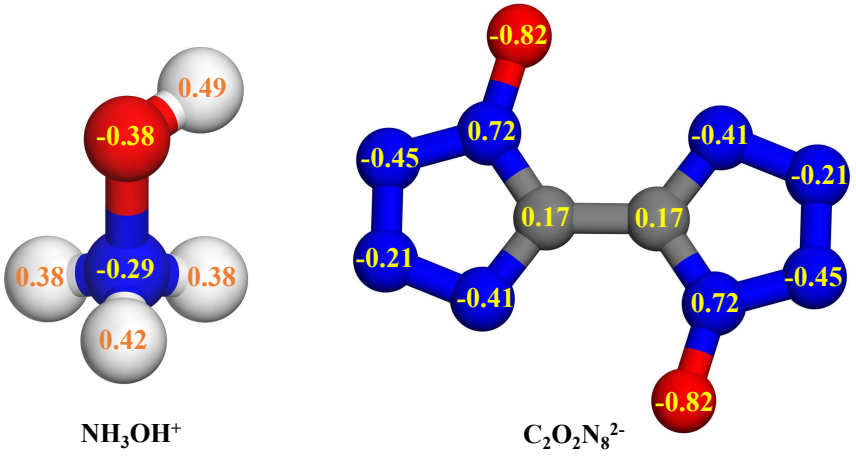

FIG. S1. Charge distribution of NH_3OH^+ and $C_2O_2N_8^{2-}$ molecules of the unit cell of the TKX-50.

To further validate the charge assignment and accuracy, we additionally derived atomic charges at varying levels of theory, including B3LYP/6-31G(d), HF/6-311G(d,p), and WB97XD/6-311G(d,p). A direct comparison of the charge distributions (Table. I below) shows that while numerical values differ slightly among the methods, the charge distributions for key functional groups—particularly the N-oxide group—remained consistent.

Additional NEMD simulations of pure TKX-50 systems using these different charge sets confirm this consistency, as shown in Fig. S2, the calculated thermal conductivity (κ) exhibits only slight variations among the charge models, while the overall trends, particularly the influence of charge distribution, remain consistent.

TABLE I. Comparison of ESP-fitted partial charges for representative atoms at different levels of theory

atom	HF/6-311G(d)	B3LYP/6-31G(d)	HF/6-311G(d,p)	WB97XD/6-311G(d,p)	Range($\max_q - min_q$)	RMSE
N1	0.72	0.74	0.72	0.81	0.09	0.053
N2	-0.45	-0.48	-0.44	-0.49	0.05	0.029
N3	-0.21	-0.22	-0.22	-0.23	0.02	0.014
N4	-0.41	-0.40	-0.41	-0.40	0.01	0.008
C1	0.17	0.11	0.17	0.11	0.06	0.049
O1	-0.82	-0.74	-0.82	-0.79	0.08	0.085
N5	-0.29	-0.28	-0.32	-0.33	0.04	0.034
H1	0.38	0.37	0.39	0.38	0.02	0.008
H2	0.38	0.37	0.39	0.38	0.02	0.008
H3	0.42	0.42	0.43	0.43	0.01	0.008
O2	-0.38	-0.35	-0.38	-0.35	0.03	0.024
H4	0.49	0.46	0.49	0.48	0.03	0.018

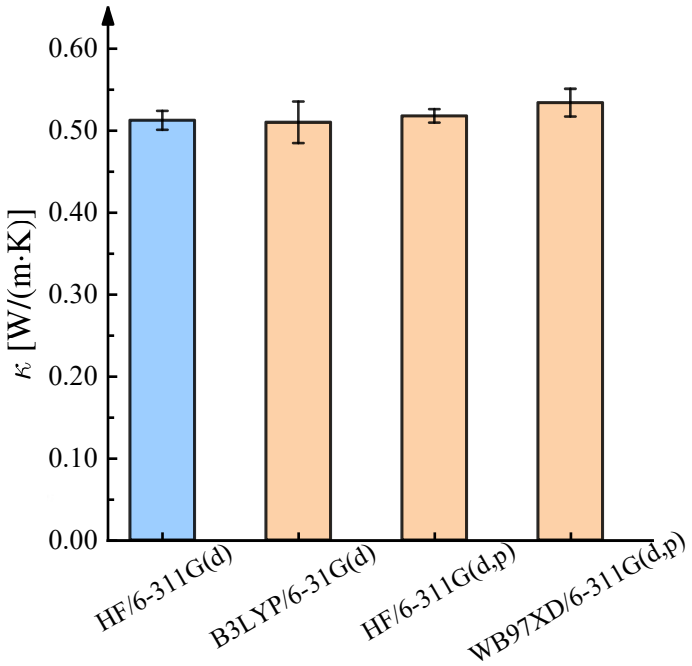

FIG. S2. Charge distribution of NH_3OH^+ and $C_2O_2N_8^{2-}$ molecules of the unit cell of the TKX-50.

To assess the compatibility of charge models with the force field, we also performed NEMD simulations of the composite system using different force fields, including COMPASS II and

Universal, while keeping the same set of ESP charges. As shown in Fig. S3, the thermal conductivity values obtained with COMPASS II (0.85 ± 0.01 W/(m·K)) and Universal (0.88 ± 0.02 W/(m·K)) differ only slightly from those obtained with COMPASS.

These small deviations arise from differences in the Lennard–Jones and bonded interaction parameters, but they do not affect the overall thermal transport trends. Therefore, the present simulations employing both fixed and customized atomic charges provide a robust estimate of the thermal conductivity.

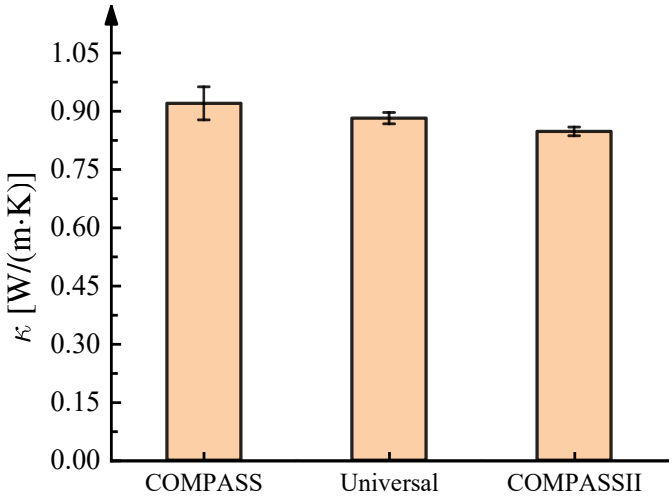

FIG. S3. Thermal conductivity comparison across different force fields with consistent HF/6-31G(d) derived charges.

II. NUMERICAL INTEGRATION AND ENERGY CONSERVATION

The velocity-Verlet integrator, a second-order symplectic method, was employed for all molecular dynamics simulations. This integrator is commonly used in molecular dynamics simulations due to its balance between accuracy and computational efficiency. To assess energy conservation at different time steps, NVE simulations were performed with time steps of 1.0 fs, 0.10 fs, and 0.01 fs, as shown in Fig. S4. The energy drift for each timestep was found to be minimal, with values of -0.0057 kcal/mol·ps, 0.000145 kcal/mol·ps, and 0.0000199 kcal/mol·ps, respectively. The cumulative relative drift (Δrel) for each time step was calculated using the following formula:

$$\Delta_{\text{rel}} = \frac{|b| \cdot t}{|\langle E \rangle|} \tag{1}$$

where b is the drift slope (in kcal/mol·ps), t is the simulation duration, and $|\langle E \rangle|$ is the average total energy. For all time steps tested, the cumulative relative drift was found to be below 10^{-4}, indicating stable energy conservation in all cases. These results confirm that a 1.0 fs timestep provides sufficient energy conservation, ensuring the reliability of the simulation results.

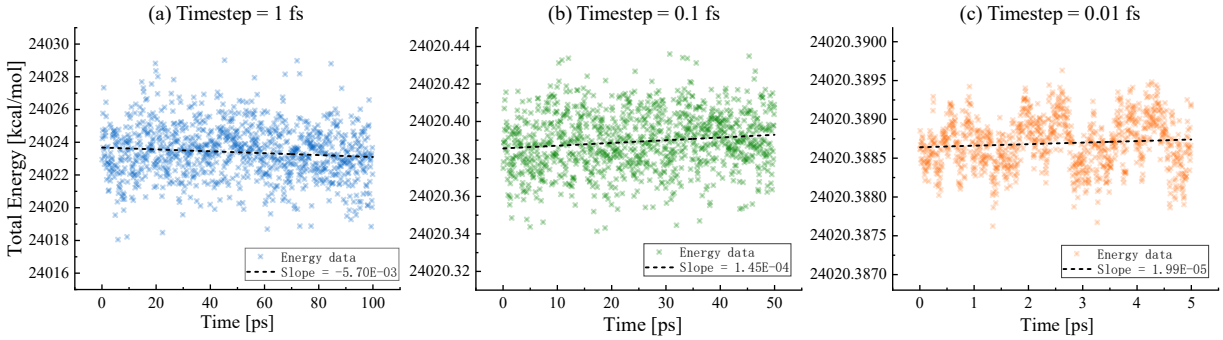

FIG. S4. Total energy during NVE simulations with different time steps.

III. TIME STEP AND VELOCITY EXCHANGE FREQUENCY IN NEMD SIMULATIONS

Fig. S5(a) shows the thermal conductivity(κ) obtained with different time steps in rNEMD simulations. From this plot, the κ for pure TKX-50 varied only slightly across the tested range. In our simulations, a time step of 1.0 fs was employed. Although a larger time step (e.g., above 1.5 fs) improves computational efficiency, it reduces system stability. Specifically, when testing with time steps of 1.6 fs and larger, significant numerical instabilities occur, including large energy fluctuations and unphysical thermodynamic behavior. For instance, the total energy suddenly increased to 50000 kcal/mol. When the time step exceeded 2.0 fs, the simulation diverged within a few steps, accompanied by atomic overlaps and bond breaking. A time step of 1.0 fs provides an optimal balance between numerical stability and computational efficiency.

Furthermore, we examined the effect of velocity exchange frequency while fixing the time step at 1.0 fs. At very low frequencies, the temperature gradient between hot and cold slabs

became too weak to determine accurately, whereas excessively high frequencies disrupted the linear temperature profile due to unrealistically large heat fluxes. As shown in Fig. **??**(b), both extremes lead to large errors in the estimated thermal conductivity. Therefore, an exchange frequency of every 200 steps was adopted.

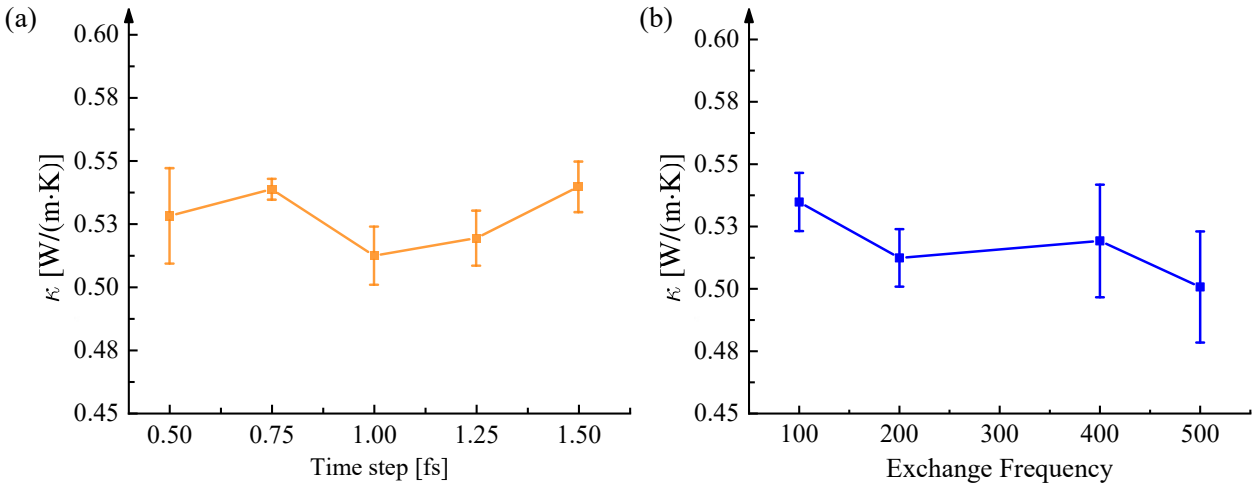

FIG. S5. Variation of thermal conductivity with time step (a) and exchange frequency (b) for pure TKX-50.

IV. VALIDATION OF VELOCITY EXCHANGE NUMBER IN NEMD SIMULATIONS

To assess the convergence of thermal conductivity for the number of energy exchanges, additional NEMD simulations were performed on pure TKX-50 using various velocity exchange numbers beyond the standard setup. As shown in Fig. S6, the calculated thermal conductivity values remained consistent across different exchange numbers. Specifically, the thermal conductivity(κ) values were 0.50, 0.52, and 0.53 W/(mK) for 1500, 2000, and 2500 exchanges, respectively, with deviations within 6%. This confirms that the selected number of exchanges is sufficient for accurate and reliable thermal conductivity estimation.

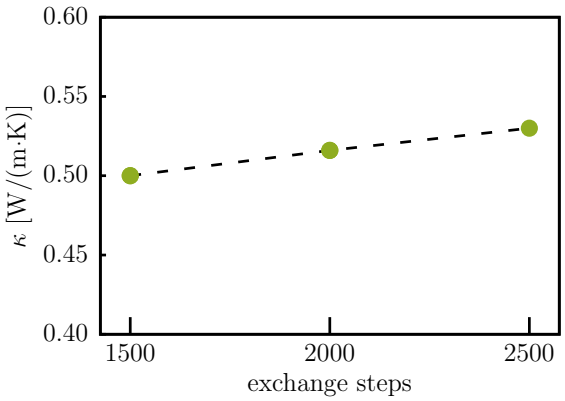

FIG. S6. Thermal conductivity of TKX-50 under different numbers of velocity exchanges.

V. PRESERVATION OF MOLECULAR ORDERING IN TKX-50 DURING SIMULATIONS

To quantify the molecular orientation and degree of order during the simulations, we used the second-order orientation parameter P_2, which is defined by the following formula:

$$P_2 = \langle \frac{3\cos^2\theta - 1}{2} \rangle \tag{2}$$

where θ is the angle between the vector (the N-oxide group in our case) and the reference direction(the c-axis). This formula provides a measure of the degree to which the molecules are aligned with the reference direction. Specifically, P_2=1 corresponds to perfect alignment (all molecules are parallel to the reference direction), P_2=0 corresponds to random orientation (no preferred alignment), and a value of P_2=-0.5 corresponds to a simulation where the feature vectors are predominantly oriented perpendicular to the reference direction.

Fig. S7 shows the molecular orientation analysis. As calculated from the standard crystal structure of TKX-50, the angle between all the N-oxide groups and the reference direction (the c-axis) was calculated to be 0.99. During the NPT simulation at the room temperature of 298 K, and after averaging over multiple trajectories, the P_2 value stabilized around 0.55, indicating that the system still maintained a good degree of molecular order. Given this molecular stability, the retained packing order could result from strong tetrazole-tetrazole interactions, which are typically seen in nitrogen-rich heterocyclic compounds. Therefore, it remains relevant to examine whether anisotropic thermal conductivity, arising from direction-dependent heat transport, is present in the system.

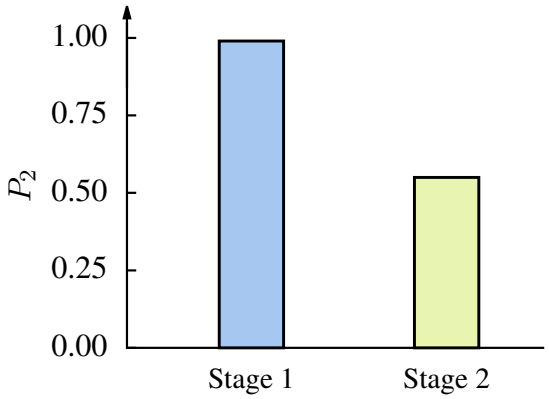

FIG. S7. Molecular orientation analysis of N-oxide groups. Stage 1 corresponds to the crystal structure with a P_2 value of 1.00. Stage 2 represents the structure during the NPT simulation, where the P_2 value stabilizes around 0.55.

VI. TEMPERATURE EFFECTS ON THERMAL TRANSPORT IN PURE TKX-50 SYSTEM

Fig. S8(a-b) presents the thermal conductivity of pure TKX-50 at various temperatures, along with the corresponding normalized heat flux profiles. The results confirm consistent heat flux equilibration across all tested temperatures, supporting the validity of the thermal conductivity calculations.

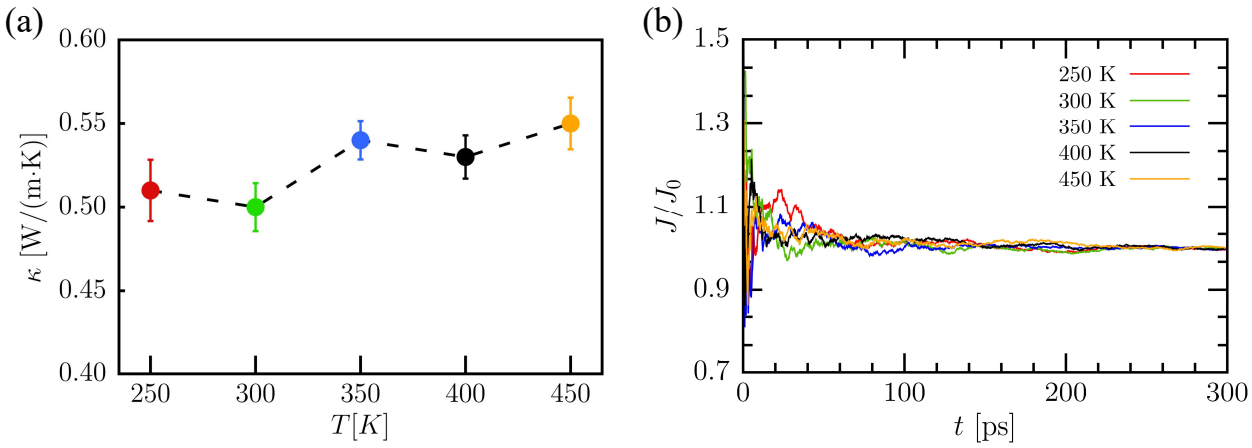

FIG. S8. (a) Variation of thermal conductivity under different temperatures. (b) Normalized heat flux J/J_0 as a function of simulation time for pure TKX-50 under different temperatures.

VII. CRYSTAL PACKING AND THERMAL ANISOTROPY

The molecular packing of TKX-50 along the a, b, and c directions is shown in Fig. S9(a-c). Subtle differences in the stacking and alignment of the molecules are evident. These structural differences are likely responsible for the observed anisotropy in thermal conductivity, as the molecular interactions along these directions vary slightly, affecting heat transport properties.

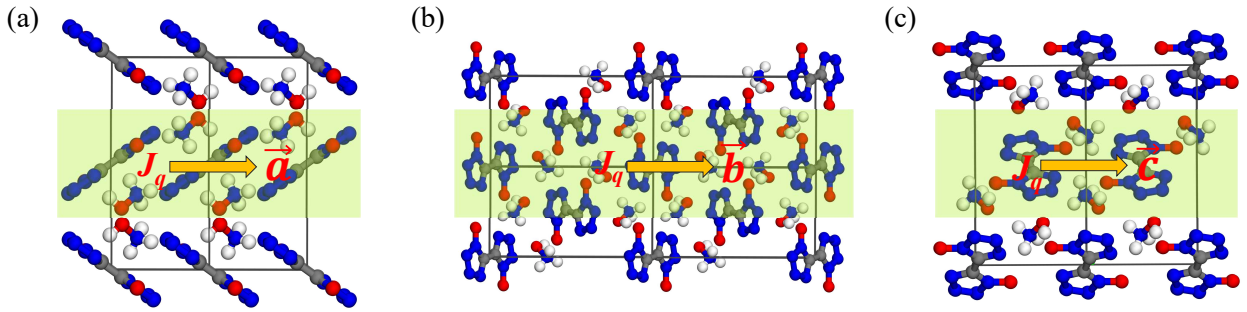

FIG. S9. Snapshot of the crystal packing along the a, b, and c directions of TKX-50. The heat flux direction (indicated by arrows) is shown as a snapshot of the transport direction in the simulations.

VIII. INFLUENCE OF MODEL SIZE ON THERMAL CONDUCTIVITY

Fig. S6 shows the thermal conductivity of compound TKX-50 calculated using three different simulation domain sizes, all with heat flux applied along the c direction. Model A (cf. Fig. S10(a)) doubled the length along the a-axis ($a = 2c$), while keeping the b-axis and c-axis lengths fixed; Model B (cf. Fig. S10(b)) doubled the length along the b-axis ($b = 2c$), while keeping the a-axis and c-axis fixed; and Model C (cf. Fig. S10(c)) doubled the lengths of all three axes compared to the original model. Due to the larger system size, the energy exchange step in the NEMD simulations was increased from 500 to 1000, allowing for more accurate simulations of heat transfer in the expanded domain. The resulting thermal conductivities, shown in Fig. S10(d), are all within 15% of the original values, demonstrating a limited size effect on thermal conductivity. In each case, a steady-state heat flux and linear temperature gradient were established, as indicated in Fig. S11-S13.

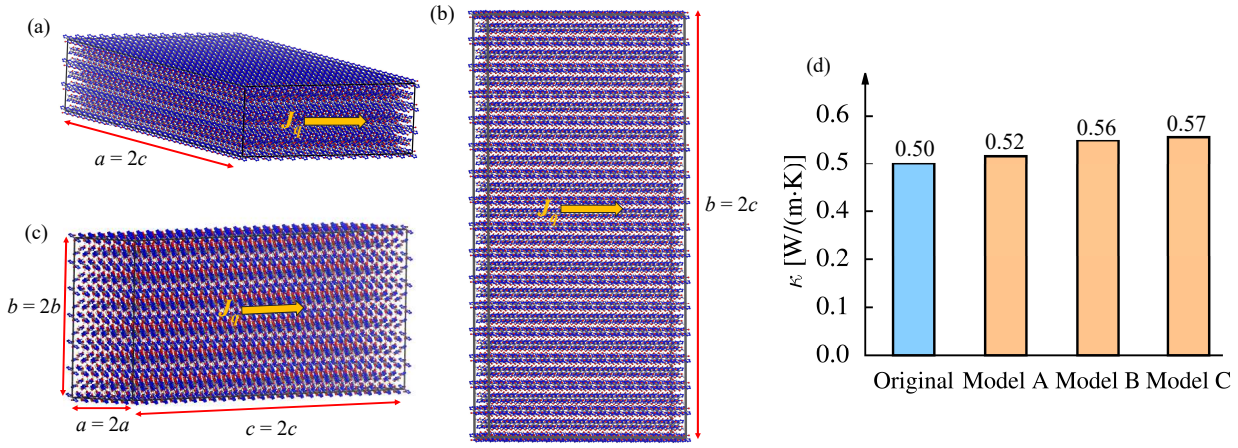

FIG. S10. Model configurations for pure TKX-50 with heat flux applied along the c-direction. (a) Model A: $a = 2c$, (b) Model B: $b = 2c$, (c) Model C: all axes doubled. (d) Thermal conductivity results for these models.

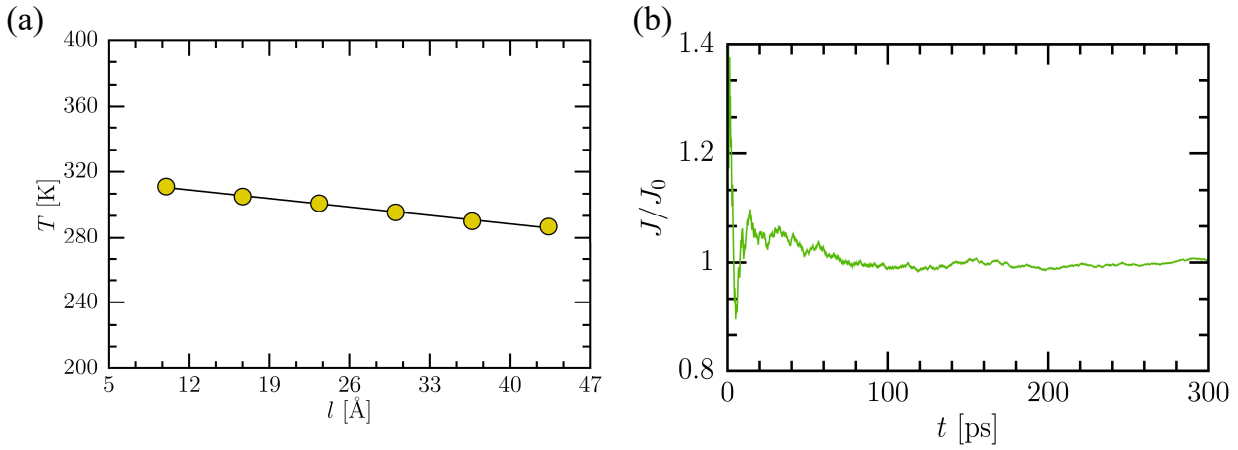

FIG. S11. Temperature gradient (a) and normalized heat flux J/J_0 over time (b) for Model A.

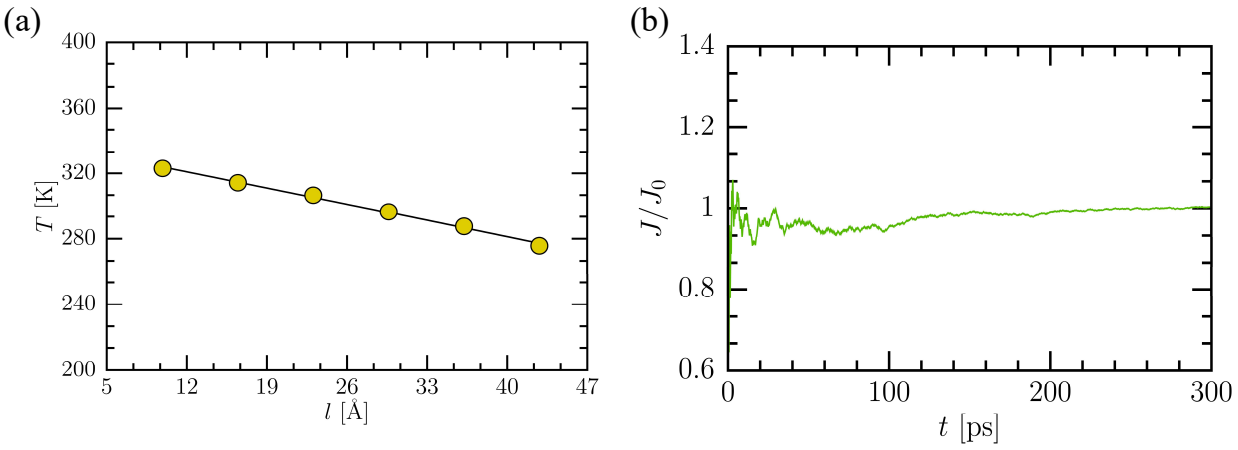

FIG. S12. Temperature gradient (a) and normalized heat flux J/J_0 over time (b) for Model B.

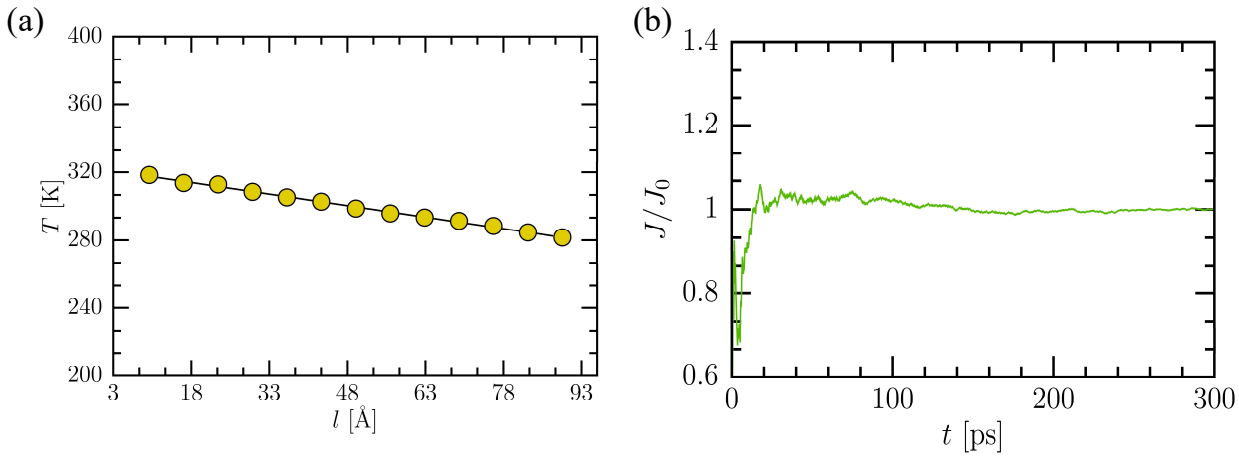

FIG. S13. Temperature gradient (a) and normalized heat flux J/J_0 over time (b) for Model C.

IX. HEAT FLUX EQUILIBRATION IN TKX-50-GRAPHENE SYSTEM

The evolution of normalized heat flux J/J_0 was analyzed in composite systems containing graphene or CNTs at different mixture ratios, confirming the reliability of thermal conductivity calculations across various filler types. In addition, for graphene-based systems, heat flux behavior was further evaluated along the c and b directions with graphene inserted either perpendicular or parallel to the transport direction, as illustrated in Fig. S14-S16.

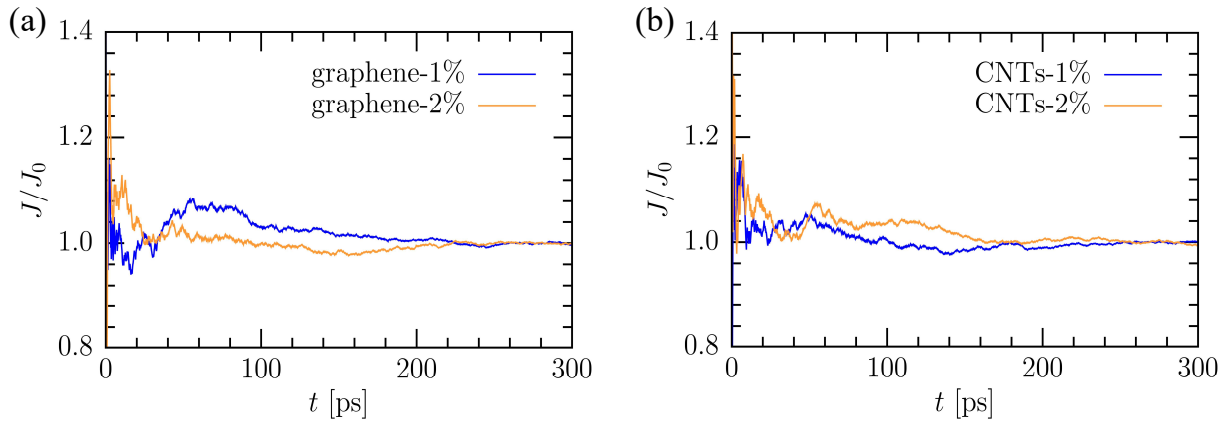

FIG. S14. Time evolution of normalized heat flux J/J_0 in systems containing (a) graphene and (b) CNTs at different mixture ratios

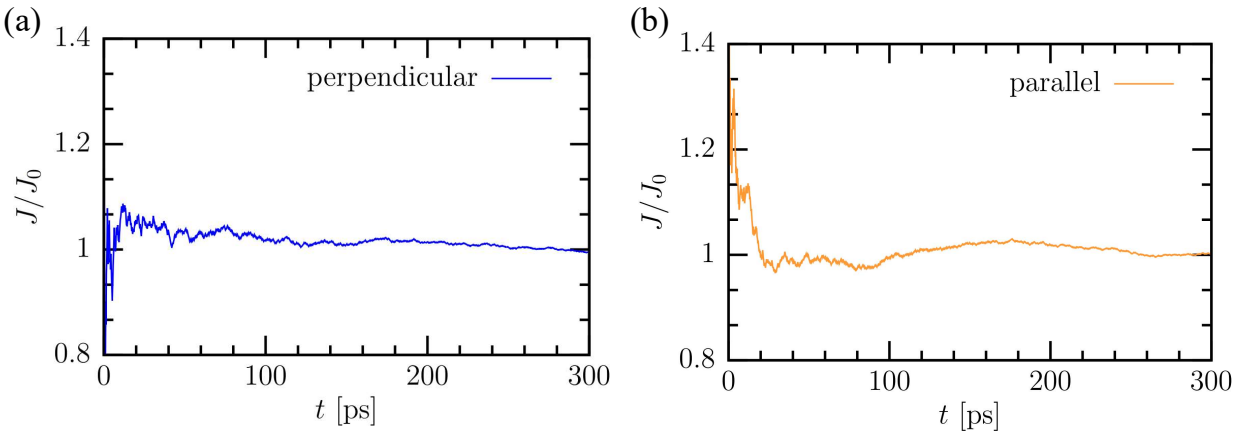

FIG. S15. The variation of the normalized heat flux J/J_0 with simulation time t for monolayer graphene-TKX-50 along the heat transfer direction c, with graphene inserted (a) perpendicular and (b) parallel to the incoming heat flux.

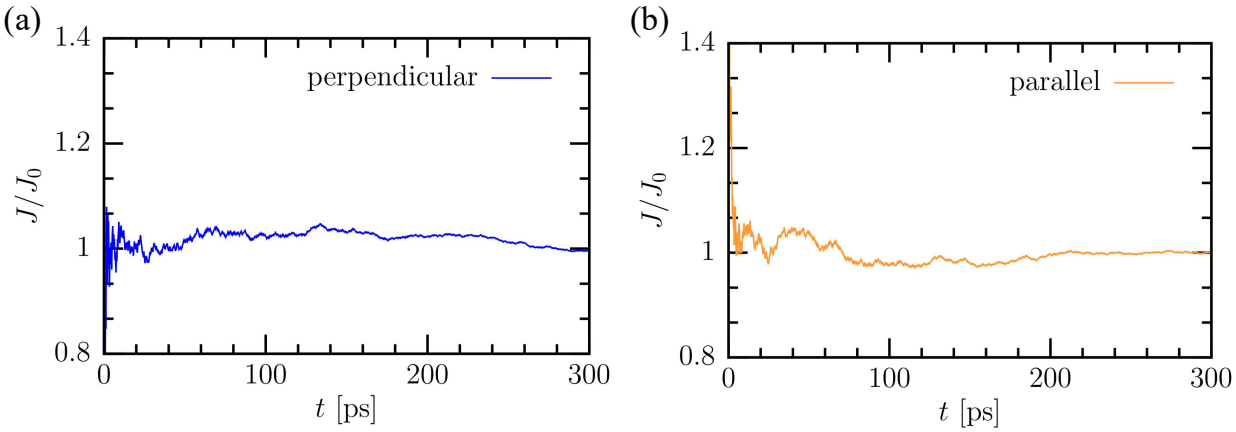

FIG. S16. The variation of the normalized heat flux J/J_0 with simulation time t for monolayer graphene-TKX-50 along the heat transfer direction b, with graphene inserted (a) perpendicular and (b) parallel to the incoming heat flux.

X. CHARGE MODEL AND GEOMETRIC EFFECTS ON TKX-50-GRAPHENE INTERACTION

Fixed atomic charges were assumed during the molecular dynamics (MD) simulations, meaning polarization effects or charge transfer between TKX-50 and graphene were not considered. The observed interaction variations were therefore attributed solely to the relative orientation of the N-oxide group in TKX-50 with respect to the graphene layer, rather than to electronic structure changes.

To investigate the potential impact of polarization, additional calculations were performed with different relative orientations of TKX-50 and graphene (perpendicular and parallel configurations), shown in Table. II, The results showed that the atomic charges in both configurations differed only slightly from the fixed-charge model (maximum per-atom difference of $|\Delta q|_{\max} \lesssim 0.13\, e$). Thus, the simulation with fixed charges still provides a good approximation of the system and can be used for thermal conductivity calculation.

TABLE II. ESP-fitted partial charges on graphene for perpendicular and parallel with respect to the TKX-50 N-oxide group.

atom	Perpendicular		atom	Parallel	
	Charge	$\|\Delta q\|$		Charge	$\|\Delta q\|$
N1	0.65	0.07	N1	0.61	0.11
N2	−0.32	0.13	N2	−0.42	0.03
N3	−0.19	0.02	N3	−0.27	0.06
N4	−0.34	0.07	N4	−0.40	0.01
C1	0.15	0.02	C1	0.21	0.04
O1	−0.79	0.03	O1	−0.71	0.11
N5	−0.30	0.01	N5	−0.30	0.01
H1	0.32	0.10	H1	0.39	0.03
H2	0.35	0.03	H2	0.38	0.00
H3	0.52	0.03	H3	0.53	0.04
O2	−0.50	0.12	O2	−0.47	0.09
H4	0.45	0.04	H4	0.45	0.04

XI. VAN DER WAALS INTERACTION BETWEEN GRAPHENE AND TKX-50

A detailed energy component analysis was performed to evaluate the interaction between TKX-50 and graphene, with a focus on van der Waals forces and electrostatic interactions. The analysis shows that the primary contribution to the interaction is from van der Waals forces, with electrostatic interactions being negligible due to the nonpolar nature of graphene(Fig. S17(a)).

Atomic-level analysis of the van der Waals potential between TKX-50 and graphene (Fig. S17) reveals that nitrogen and oxygen atoms from both the cation and anion of TKX-50 are the major contributors to the van der Waals attraction, with the contribution from hydrogen atoms being minimal. The results confirm the dominance of van der Waals forces at the interface.

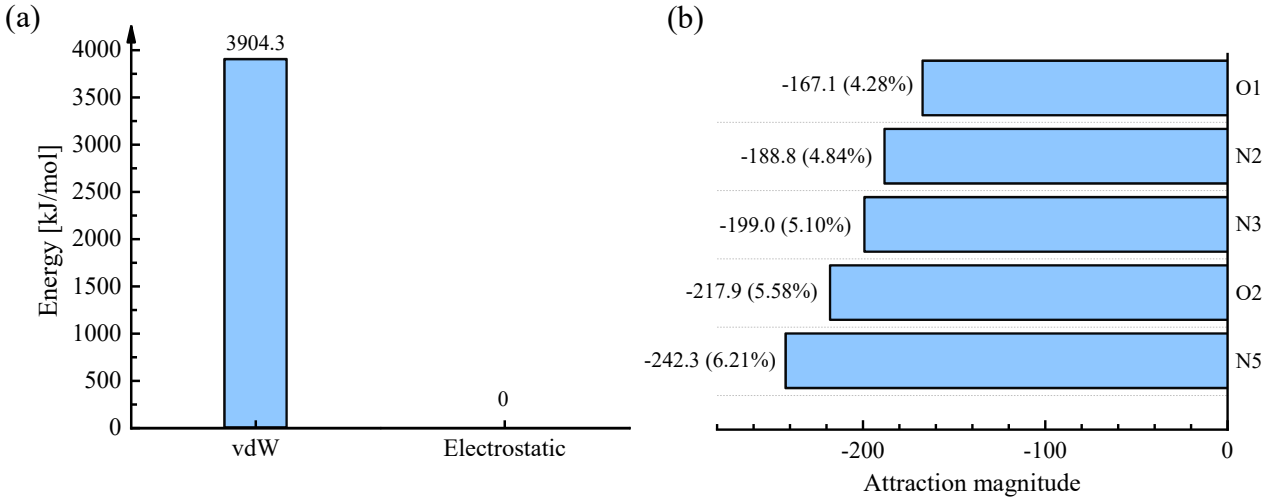

FIG. S17. Interfacial non-bonded interactions between TKX-50 and graphene and atomic-scale vdW attraction.

[1] X.-H. JuQ and J.-S. Zhao, Foundations of Crystallography **5**, 0 (2018).